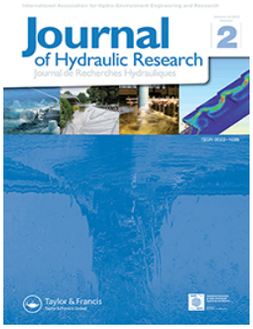

Journal of Hydraulic Research

ISSN: 0022-1686 (Print) 1814-2079 (Online) Journal homepage: http://www.tandfonline.com/loi/tjhr20

Spatially-averaged momentum fluxes and stresses in flows over mobile granular beds: a DNS-based study

Bernhard Vowinckel, Vladimir Nikora, Tobias Kempe & Jochen Fröhlich Professor

To cite this article: Bernhard Vowinckel, Vladimir Nikora, Tobias Kempe & Jochen Fröhlich Professor (2017) Spatially-averaged momentum fluxes and stresses in flows over mobile granular beds: a DNS-based study, Journal of Hydraulic Research, 55:2, 208-223, DOI: 10.1080/00221686.2016.1260658

To link to this article: http://dx.doi.org/10.1080/00221686.2016.1260658

Journal of Hydraulic Research Vol. 55, No. 2 (2017), pp. 208–223
http://dx.doi.org/10.1080/00221686.2016.1260658

Research paper

Spatially-averaged momentum fluxes and stresses in flows over mobile granular beds: a DNS-based study

BERNHARD VOWINCKEL[†], Postdoctoral Fellow, *Institute of Fluid Mechanics, Technische Universität Dresden, Dresden, Germany*
Email: vowinckel@engineering.ucsb.edu (author for correspondence)

VLADIMIR NIKORA (IAHR Member) Professor, *School of Engineering, University of Aberdeen, Aberdeen, Scotland*
Email: v.nikora@abdn.ac.uk

TOBIAS KEMPE, Researcher, *Institute of Fluid Mechanics, Technische Universität Dresden, Dresden, Germany*
Email: tobias.kempe@tu-dresden.de

JOCHEN FRÖHLICH, Professor, *Institute of Fluid Mechanics, Technische Universität Dresden, Dresden, Germany*
Email: jochen.froehlich@tu-dresden.de

ABSTRACT
Based on direct numerical simulations, the paper investigates momentum fluxes and hydrodynamic stresses within and above a mobile granular bed in a turbulent open-channel flow laden with monodisperse spherical particles. Two simulation scenarios are considered: one with partially mobilized particles ("heavy" particles) and another with all particles in motion ("light" particles). The momentum fluxes were computed as temporal and spatial averages following the double-averaging methodology for rough-bed flows. The analysis, hence, allows the DNS data to be convoluted in a rigorous way to provide detailed description and quantification of the physical mechanisms involved in momentum exchanges. In particular, it was found that heavy particles create streamwise bedforms causing heterogeneity in the spanwise direction. This yields significant form-induced momentum fluxes that cannot be neglected. For both scenarios, the mobile particles take up a substantial amount of the momentum supplied, which ultimately increases the hydraulic resistance of the channel. These effects enhance and stabilize secondary flows in the channel.

Keywords: Bedforms; direct numerical simulations; double-averaging methodology; particle-laden flows; secondary currents; turbulence–sediments interactions

1 Introduction

Understanding, predicting, and measuring sediment transport in open-channel flows is an important task in many hydraulic and environmental applications such as the management of streams and reservoirs, maintenance of sewerage systems, or optimizing pipelines for pneumatic conveying. The physical processes associated with sediment transport are diverse and occur at different temporal and spatial scales. Scientists and engineers have tried to understand and model these processes for more than a century (e.g. Dey, 2014; Graf, 1996; Mavis, Ho, Tu, Liu, & Soucek, 1935; Williams, 1937; Yalin & Ferreira da Silva, 2001). However, many aspects of sediment transport are still poorly understood and progress in deriving sound concepts for modelling and predicting sediment transport has been slow. The main reason for this is likely to be associated with the experimental difficulties in obtaining high-resolution data under challenging conditions of mobile-bed flows. This is especially true for situations where sediment preferentially accumulates, which is commonly known as particle clustering (Seminara, 2010; Toschi & Bodenschatz, 2009). On top of that, understanding of sediment phenomena requires sound quantitative frameworks for describing sediment transport and associated turbulent flow. Thus, the research in this area remains very active and intensive efforts have been undertaken recently to address these problems (e.g. Ancey & Heyman, 2014; Ferreira, Franca, Leal, & Cardoso, 2012; Furbish, Haff, Roseberry, & Schmeeckle, 2012; Lajeunesse, Malverti, & Charru, 2010; Ma et al., 2015; Nikora, Ballio, Coleman, & Pokrajac, 2013, among others).

Received 21 September 2015; accepted 27 October 2016/Open for discussion until 31 October 2017.

[†] *Current address:* Department of Mechanical Engineering, University of California, Santa Barbara, USA

ISSN 0022-1686 print/ISSN 1814-2079 online
http://www.tandfonline.com

The basis of the present work is high-resolution direct numerical simulations (DNS) of particle-laden flow over a rough bed presented in (Vowinckel & Fröhlich, 2012; Vowinckel, Kempe, Fröhlich, & Nikora, 2012), where the fully coupled system is considered (e.g. Balachandar & Eaton, 2010). The simulations resolved all relevant scales down to the sub-particle scale by employing the immersed boundary method (IBM). Hence, with sufficient computing power available, this numerical approach is a powerful tool for generating data for mobile-bed conditions. A systematic analysis of the generated DNS data is carried out following an approach known as the double-averaging methodology (DAM), which is based on temporal and spatial averaging in multiphase systems (e.g. Nikora, McEwan, et al., 2007; Nikora, McLean, et al., 2007; Nikora et al., 2013). It has been shown that this approach is a promising tool for integrating complex particle–fluid interactions in fluvial systems (e.g. Nikora & Rowiński, 2008). The present study, indeed, illustrates that this approach is useful for rigorous coupling of sediment and flow motions as well as for up-scaling of the physical processes occurring at grain or bedform scales. Application of this methodology for mobile-bed conditions, however, remains challenging as it requires high-resolution data in both space and time. In a companion paper (Vowinckel, Nikora, Kempe, & Fröhlich, 2017), the DAM was successfully applied to DNS data in the analysis of the momentum balance in a turbulent flow over a mobile granular bed. Vowinckel, Nikora, et al. (2017) provide details on the space-time sampling and averaging strategies and report a detailed assessment of the key terms of the double-averaged momentum balance. The goal of the present study is to assess governing physical mechanisms by means of spatially-averaged momentum fluxes and link them to the typical flow and bed surface patterns observed in the simulations to gain a deeper insight into the fluid–particle interactions. Utilizing the DAM, our approach allows detailed assessment of particle distribution and momentum fluxes in the channel at a local (grain) scale. The obtained data is then exploited to assess a full global momentum balance and to investigate dominant flow features such as secondary currents.

The paper is structured as follows. First, the numerical method and the computational scenarios are briefly summarized in Sections 2 and 3. Then, in Section 4 the governing averaging operators are outlined as well as an integral formulation for the double-averaged momentum balance and the spatially-averaged momentum fluxes. Section 5 presents estimates of the spatially-averaged momentum fluxes accounting for both local effects at the grain scale and global flow properties. In addition, highly resolved wall-normal profiles of the stresses within and over mobile granular bed are provided. The paper closes with an analysis of the secondary currents that typically emerge in channels with low sediment transport rates when streamwise ridges are formed (Allen, 1982; Nezu & Nakagawa, 1993). The results clearly highlight the capability of the DAM to condense the detailed information into physically meaningful quantities and give new insight into the complex mechanisms involved in sediment transport.

2 Numerical method

2.1 *Immersed boundary method and collision modelling*

The DNS data analysed in the present study were generated using fully-resolved simulations of particle-laden flows over a horizontal bed using the IBM. This approach has become the method of choice when the data at the sub-grain scale are required (Kempe & Fröhlich, 2012a; Uhlmann, 2005; Vowinckel, Jain, Kempe, & Fröhlich, 2016). A full description of the DNS employed in the simulations can be found in Kempe and Fröhlich (2012a) and Kempe, Vowinckel, and Fröhlich (2014), and therefore only a brief summary is provided here. The unsteady three-dimensional Navier–Stokes equations for incompressible fluid are used:

$$\frac{\partial \mathbf{u}}{\partial t} + \nabla \cdot (\mathbf{u}\mathbf{u}) = \frac{1}{\rho_f} \nabla \cdot \boldsymbol{\tau} + \mathbf{f} + \mathbf{f}_{IBM} \tag{1}$$

$$\nabla \cdot \mathbf{u} = 0 \tag{2}$$

where $\boldsymbol{\tau}$ is the fluid stress tensor:

$$\tau = -p\,\mathrm{I} + \rho_f \nu_f \nabla \mathbf{u} \tag{3}$$

and $\mathbf{u} = (u_1, u_2, u_3)^T = (u, v, w)^T$ is the velocity vector, ρ_f is the fluid density, p is pressure, ν_f is the kinematic viscosity, $\mathbf{f}_{IBM}$ is a source term introduced as explained below, and $\mathbf{I}$ is the identity matrix. A Cartesian coordinate system is employed, where x, y, and z are the streamwise, wall-normal, and spanwise coordinates, respectively. The term $\mathbf{f} = (f_x, 0, 0)^T$ represents an artificial volume force driving the mean flow in the streamwise direction and is adjusted so as to impose a given bulk Reynolds number.

The spatial discretization of Eqs (1) and (2) is performed by a second-order finite-volume scheme on a fixed Cartesian grid with staggered positions of the variables. The convective terms are treated with an explicit Runge–Kutta three-step method and the viscous terms with an implicit Crank–Nicolson scheme. The divergence-free velocity field at the end of each Runge–Kutta sub-step is obtained by the solution of a Poisson equation for the pressure correction and subsequent projection. The dispersed phase is represented by an enhanced IBM, which extends the method of Uhlmann (2005).

To model particle–particle contacts, the adaptive collision model (ACM) is used (Kempe & Fröhlich, 2012b). The ACM accounts for the relevant mechanisms and forces that have to be modelled during the collision process: short-range lubrication forces, normal forces during surface contact (by imposing the correct restitution coefficient), and tangential forces due to friction between particles. The ACM was validated in great detail in Kempe and Fröhlich (2012b). Previous investigations of particle transport in a similar setup as presented here showed that

the ACM yields realistic results which are in agreement with experimental evidence (Kempe et al., 2014; Vowinckel et al., 2012, 2014).

2.2 *Computational set-up*

The computational set-up of the studied horizontal flow is the same as described in Vowinckel et al. (2012) and Vowinckel and Fröhlich (2012). The considered free-surface flow features periodic boundary conditions in streamwise and spanwise direction. A free-slip condition is employed at the top boundary. The sediment bed is modelled by one layer of 6696 fixed hexagonally packed mono-disperse spheres of diameter D. The origin of the vertical coordinate y was set at the crest of the fixed spheres. The computational domain is $\Omega = [0;\ 12\,H] \times [-D; H] \times [0; 6H]$ where H is the channel height. The Reynolds number $\mathsf{R_b} = U_b\ H/\nu_f$ is 2700 for an unladen flow, where U_b is the bulk velocity. The friction velocity is defined as $u_\tau = \sqrt{\tau_w/\rho_f}$, where the wall shear stress τ_w is obtained by extrapolating the total shear stress of an unladen flow down to $y = 0$. The shear velocity of the unladen flow is used here to provide estimates of the roughness regime, the grid resolution, and an *a priori* estimate of the Shields parameter (Shields, 1936):

$$\mathsf{Sh} = \frac{u_\tau^2 \rho_f}{(\rho_p - \rho_f)gD} = \frac{u_\tau^2}{\rho' gD} \tag{4}$$

for the particle-laden case, where ρ_p is the particle density and $\rho' = (\rho_p - \rho_f)/\rho_f$. Note that *a priori* quantities are not used for scaling flow parameters. The resulting particle Reynolds number $\mathsf{D}^+ = u_\tau D/\nu_f = 19.2$ indicates that the simulated flow corresponds to the transitionally rough hydraulic regime (Schlichting, 1960). The present set-up is based on the experimental design of Cameron, Nikora, and Coleman (2008), who used glass spheres of diameter $D = 11.1$ mm and oil as a fluid leading to the Reynolds numbers similar to our study. Each particle is resolved with 22 points per diameter resulting in a resolution $\Delta_x^+ = \Delta_x u_\tau/(\nu_f) = 0.86$ in terms of wall units where $\Delta_x = \Delta_y = \Delta_z$ are the cell sizes of the isotropic, equidistant mesh in streamwise, wall-normal, and spanwise directions, respectively. This results in a total number of 645 million grid cells.

3 Simulation scenarios

3.1 *Key parameters*

To assess the momentum fluxes and the particle–fluid interactions in flows over mobile granular beds, two distinct simulation scenarios were studied with different bed mobility, representing partially and fully mobilized conditions. In both scenarios, 2000 mobile particles of the same diameter as the particles of the fixed bed were released in the outer flow. The first scenario corresponds to near-critical bed conditions (case *HP*: "heavy particles"), while the second scenario corresponds to a mobile bed (case *LP*, "light particles"). The bedload transport rates for the two cases are $\dot{m}_{\mathrm{sed}}/\dot{m}_{\mathrm{f}} = 0.0024$ and $\dot{m}_{\mathrm{sed}}/\dot{m}_{\mathrm{f}} = 0.0098$, respectively, where $\dot{m}_{\mathrm{sed}}$ is the total mass flux of sediment (Ballio, Nikora, & Coleman, 2014) and $\dot{m}_{\mathrm{f}}$ is the fluid mass flux. The Shields parameters are $\mathsf{Sh}/\mathsf{Sh}_{\mathrm{crit}} = 0.7$ and $\mathsf{Sh}/\mathsf{Sh}_{\mathrm{crit}} = 2.2$, respectively, where $\mathsf{Sh}_{\mathrm{crit}} = 3.4 \times 10^{-2}$ is the nominal critical threshold of incipient motion according to Shields (1936). After an initialization period of $40T_b$ (case *HP*) and $20T_b$ (case *LP*) to reach steady-state conditions, the simulations were run for the total simulation time of 175 T_b (case *HP*) and 134 T_b (case *LP*), where $T_b = U_b/H$ is the bulk time unit. Preliminary analysis showed that the generated data are sufficient for obtaining fairly converged first and second-order statistics in the major part of the simulation domain (Vowinckel, Nikora, et al., 2017). In the following, a summary of the key flow features of the two scenarios are given recapping the preliminary analyses presented in Vowinckel et al. (2012) and Vowinckel and Fröhlich (2012).

3.2 *Scenario with heavy particles (HP)*

The particles in scenario *HP* are partially mobilized and form some typical patterns. In particular, streamwise clusters of resting particles can be observed in Fig. 1 (particles coloured by their velocity $\mathbf{u}_p$). These clusters align in the streamwise direction and induce large regions of low speed fluid (visualized in blue in Fig. 1a) due to the particle velocities being orders of magnitudes smaller than the fluid velocity in this region. A similar observation is reported for laboratory experiments at low transport rates, where ridges with an average spanwise spacing of $2H$ are found (e.g. Allen, 1982; Karcz, 1966; Nezu & Nakagawa, 1993; Shvidchenko & Pender, 2001; Yalin & Ferreira da Silva, 2001). In these references, it is argued that between the ridges two counter-rotating cells of secondary flow develop, sweeping moving particles out of the troughs towards the ridges. The ridges of the *HP* simulation scenario show a very similar pattern as observed in the experiments (Fig. 1).

The particle clusters develop to different extents in the streamwise direction, keeping at the same time an average spacing of $2H$ in the spanwise direction. The most pronounced cluster emerges at $z \approx 2H$ and spans over the entire streamwise extent of the channel. A large cluster (but smaller than the previous) is also visible at $z \approx 0H$. Another cluster with a rather disturbed pattern can be identified at $z \approx 4H$. In addition, there is some irregularity in the overall pattern, with a number of scattered, small-sized particle clusters. The three observed large scale particle clusters, however, clearly introduce spatial heterogeneity in the sediment bed topography in both streamwise and spanwise directions.

3.3 *Scenario with light particles (LP)*

Contrary to the *HP* scenario, the light particles do not form well-defined clusters at flow scales. These particles travel with a

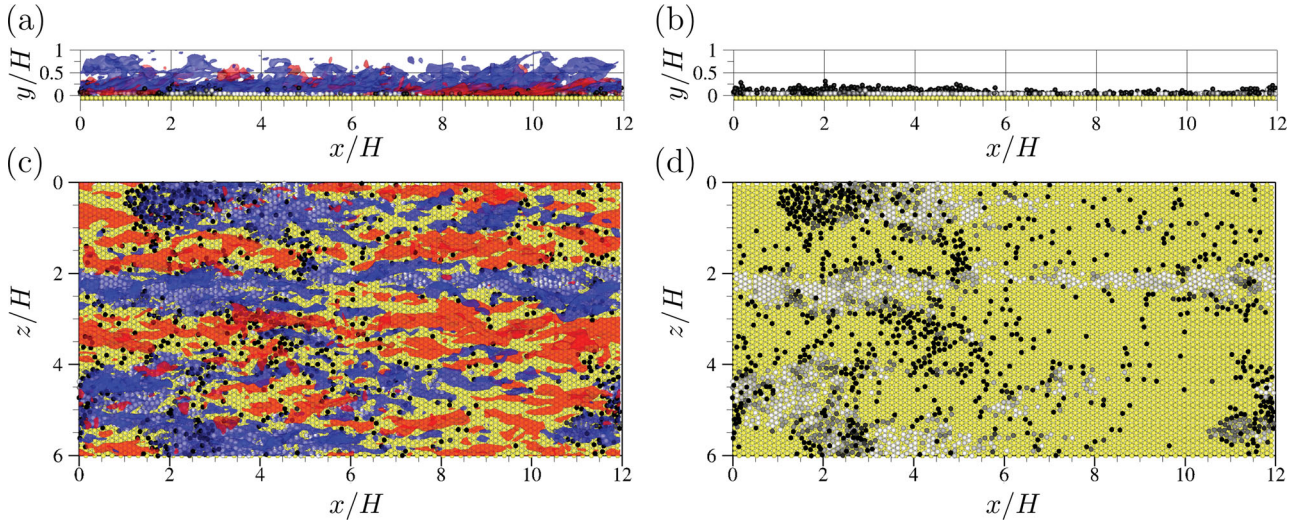

Figure 1 Snapshots of scenario *HP*. (a) Side view of coherent structures visualized with iso-surfaces of instantaneous velocity fluctuations with $u'/U_b = -0.3$ in blue and $u'/U_b = 0.3$ in red. (b) Same as (a) but without fluid information. (c) Same as (a) viewed from the top. (d) Same as (b) viewed from the top. Particles in yellow: fixed; white: $|\mathbf{u}_p| < u_\tau$, black: $|\mathbf{u}_p| \geq u_\tau$ (pictures are taken from Vowinckel, Nikora, et al., 2017)

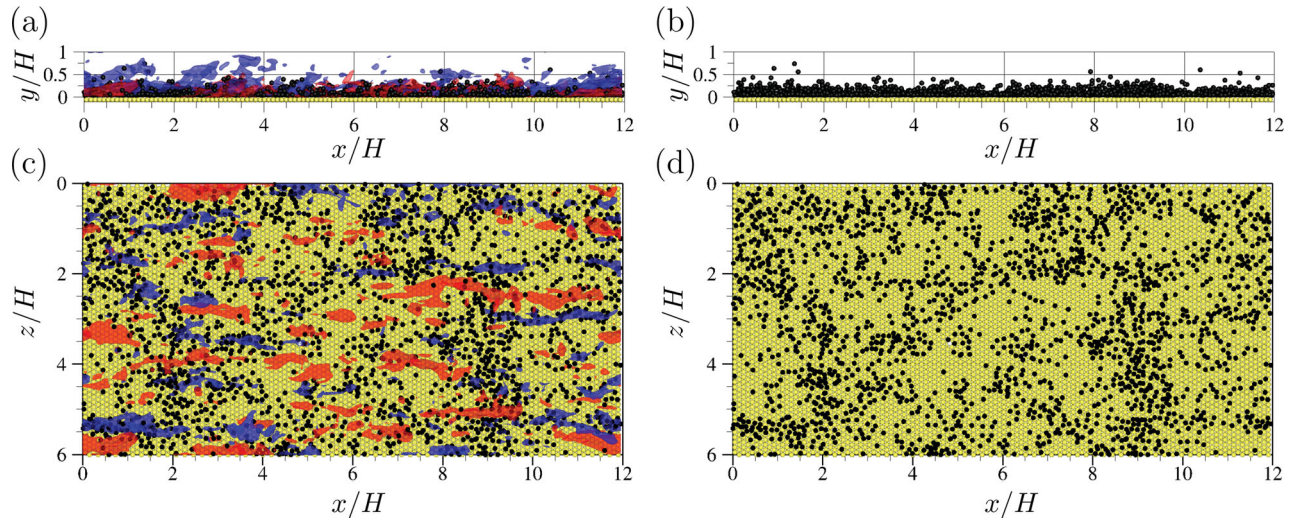

Figure 2 Snapshots of scenario *LP* (colouring as in Fig. 1). (a) Side view of coherent structures. (b) Same as (a) but without fluid information. (c) Same as (a) viewed from the top. (d) Same as (b) viewed from the top (pictures taken from Vowinckel, Nikora, et al., 2017)

significant streamwise velocity over the fixed bed (Fig. 2). It has been shown in detail by Vowinckel et al. (2012) that the fairly uniform distribution of particle kinetic energy prevents formation of reasonably stable clusters of light particles during the simulation time. Hence, this situation yields a fairly even distribution of the particles and no clusters of resting particles are observed.

4 Integral formulation of the double-averaging methodology

4.1 *Double-averaged quantities*

The present analysis was performed on the basis of the DAM for flows over mobile granular beds (Nikora et al., 2013). The DAM employs averaging operators similar to those used in studies of porous-media flows and multiphase flows (e.g. Gray & Lee, 1977). A starting point is the distinction between the two phases, solid and liquid, by a clipping function equal to 1 in the fluid and 0 otherwise. The consecutive time-space averaging operator for scalar fluid quantities θ can be defined as:

$$\langle \bar{\theta}^s \rangle^s = \frac{1}{V_0}\frac{1}{T_0}\int_{V_0}\int_{T_0} \theta(x^*, t^*)\,\gamma(x^*, t^*)\,\mathrm{d}t^*\mathrm{d}V^* = \phi_{Vm}\langle \phi_T \bar{\theta} \rangle \tag{5}$$

Here, an overbar denotes time averaging, angular brackets indicate spatial averaging, V_0 is the total volume of the averaging domain, T_0 is the total averaging time, and $\phi_T = T_f/T_0$ is the time porosity where T_f is the time during which a given location is occupied by fluid. The parameter $\phi_{Vm} = V_m/V_0$ is the space porosity where V_m is the volume within V_0 occupied by fluid (even briefly) within the total averaging time T_0. The operators $\bar{\theta}$ and $\langle\theta\rangle$ (without any sub- and superscripts)

denote the so-called intrinsic averaging over sub-domains that are actually occupied by fluid. The superscript s denotes the superficial average over the entire volume V_0 and/or entire averaging time T_0. As a consequence, the total porosity of the double-averaged mobile granular bed can be defined as $\phi_{VT} = \phi_{Vm}\,\langle\phi_T\rangle$.

The averaging operator of Eq. (5) is to be distinguished from the intrinsic averaging operator:

$$\langle\bar{\theta}\rangle = \frac{1}{V_m}\frac{1}{T_f}\int_{V_0}\int_{T_0}\theta(x^*,t^*)\,\gamma(x^*,t^*)\;\mathrm{d}t^*\mathrm{d}V^* \tag{6}$$

which averages over time T_f and volume V_m when a point is actually occupied by the fluid. Note that the intrinsically and superficially averaged quantities are connected via the porosities (e.g. $\bar{\theta}^s = \phi_V\bar{\theta}$ or $\langle\bar{\theta}\rangle^s = \phi_V\langle\theta\rangle$). The averaging operators of Eqs (5) and (6) give rise to a modified Reynolds decomposition for intrinsic quantities, since deviations in both time and space are possible:

$$\theta = \overline{\theta} + \theta', \quad \bar{\theta} = \langle\bar{\theta}\rangle + \tilde{\bar{\theta}} \tag{7}$$

In Eq. (7), the prime indicates a deviation of the instantaneous value from the time-averaged quantity and the tilde indicates deviation of the time-averaged value from its spatially averaged counterpart.

The averaging time was chosen to be the total simulation time (but excluding the initialization period mentioned in Section 3.1), to maximize statistical convergence. Two options for spatial averaging were explored: a "local" averaging domain of volume:

$$V_{0,2} = L_x\Delta_y\,2D \tag{8}$$

covering the entire streamwise extent of the computational domain L_x but well resolving the spanwise heterogeneity; and a "global" averaging domain of volume:

$$V_{0,1} = L_x\Delta_y L_z \tag{9}$$

covering the entire streamwise L_x and spanwise extents L_z, of the computational domain. The wall-normal extent of both averaging domains (Eqs (8) and (9)) is chosen to be the numerical grid cell size of the DNS in wall-normal direction (Δ_y) to guarantee a proper resolution of the wall-normal gradients for evaluation of the DAM-based quantities. In the following, averages using Eq. (8) are referred to as "local", whereas averages using Eq. (9) are named "global".

4.2 *Integral formulation for global averages*

The bulk momentum balance of the present numerical set-up can be assessed by the integral formulation of the double-averaged momentum balance. A starting point is the double averaged Navier–Stokes equations for mobile bed conditions as proposed by Nikora et al. (2013) and employed in Vowinckel, Nikora, et al. (2017):

$$\begin{aligned}
&\underbrace{\frac{\partial\phi_{Vm}\langle\phi_T\bar{u}_i\rangle}{\partial t}}_{1} + \underbrace{\frac{\partial\phi_{Vm}\langle\phi_T\rangle\langle\bar{u}_i\rangle\langle\bar{u}_j\rangle}{\partial x_j}}_{2} \\
&= \underbrace{\phi_{Vm}\langle\phi_T\bar{f}_i\rangle}_{3} - \frac{1}{\rho_f}\underbrace{\frac{\partial\phi_{Vm}\langle\phi_T\bar{p}\rangle}{\partial \mathrm{x_i}}}_{4} \\
&\quad - \underbrace{\frac{\partial\phi_{Vm}\langle\phi_T\overline{u_i'u_j'}\rangle}{\partial x_j}}_{5} - \underbrace{\frac{\partial\phi_{Vm}\langle\phi_T\tilde{\bar{u}}_i\tilde{\bar{u}}_j\rangle}{\partial x_j}}_{6} \\
&\quad + \underbrace{\frac{\partial}{\partial x_j}\left(\phi_{Vm}\left\langle\phi_T\nu_f\overline{\frac{\partial u_i}{\partial x_j}}\right\rangle\right)}_{7} \\
&\quad - \underbrace{\frac{\partial\phi_{Vm}\langle\phi_T\tilde{\bar{u}}_i\rangle\langle\bar{u}_j\rangle}{\partial x_j}}_{8} - \underbrace{\frac{\partial\phi_{Vm}\langle\phi_T\tilde{\bar{u}}_j\rangle\langle\bar{u}_i\rangle}{\partial x_j}}_{9} \\
&\quad + \underbrace{\frac{1}{\rho_f}\frac{1}{V_0}\overline{\iint_{S_{int}} p\,n_i\mathrm{d}S}^{s}}_{10} - \underbrace{\frac{1}{V_0}\overline{\iint_{S_{int}}\left(\nu_f\frac{\partial u_i}{\partial x_j}\right)n_j\,\mathrm{d}S}^{s}}_{11}
\end{aligned} \tag{10}$$

where the first and second terms represent local and convective acceleration, the third term is the momentum supply, the fourth term is the pressure gradient, the fifth, sixth, and seventh terms are contributions from turbulent, form-induced, and viscous stresses, respectively. The eighth and ninth terms are stress terms related to potential spatial correlations between temporal porosity and time-averaged velocities. Finally, the 10th and 11th terms represent pressure drag and viscous friction at the fluid–particle interfaces S_{int}, where n_i is the unit vector normal to the particle surface and directed into the fluid.

The globally"-averaged momentum balance can be used to obtain spatially-averaged momentum fluxes by integrating Eq. (10) in the vertical direction, from an elevation y to the upper boundary of the simulation domain. The free-slip boundary condition imposed at the top of the domain means that $\frac{\partial u}{\partial y} = \frac{\partial w}{\partial y} = 0$ and $v = 0$. Since the derivatives in the x- and z-directions of the globally averaged quantities vanish due to the periodic boundary conditions, only terms with indices $i = 1$ and $j = 2$ may differ from zero. This yields:

$$\begin{aligned}
&-\underbrace{\phi_{Vm}\langle\phi_T\rangle\langle\bar{u}\rangle\langle\bar{v}\rangle}_{2} \\
&= \underbrace{\bar{f}_x\int_y^H\phi_{Vm}\langle\phi_T\rangle\mathrm{d}y^*}_{3} + \underbrace{\phi_{Vm}\langle\phi_T\overline{u'v'}\rangle}_{5} + \underbrace{\phi_{Vm}\langle\phi_T\tilde{\bar{u}}\tilde{\bar{v}}\rangle}_{6} \\
&\quad - \underbrace{\phi_{Vm}\left\langle\phi_T\nu_f\overline{\frac{\partial u}{\partial y}}\right\rangle}_{7} + \underbrace{\phi_{Vm}\langle\phi_T\tilde{\bar{u}}\rangle\langle\bar{v}\rangle}_{8} + \underbrace{\phi_{Vm}\langle\phi_T\tilde{\bar{v}}\rangle\langle\bar{u}\rangle}_{9}
\end{aligned}$$

$$+\underbrace{\int_y^H \frac{1}{\rho_f}\frac{1}{V_0}\overline{\iint_{S_{\text{int}}} p n_x dS}^{s}\,\mathrm{d}y^*}_{10}$$
$$-\underbrace{\int_y^H \frac{1}{V_0}\overline{\iint_{S_{int}} \left(\nu_f \frac{\partial u_i}{\partial x_j}\right) n_y \,\mathrm{d}S}^{s}\,\mathrm{d}y^*}_{11} - \underbrace{\int_y^H \frac{\partial \phi_{Vm}\langle\phi_T\bar{u}\rangle}{\partial t}\mathrm{d}y^*}_{1} \tag{11}$$

where $n_x = n_1$ and $n_y = n_2$, as defined in Eq. (10). The integrated terms in Eq. (11) represent momentum fluxes of different origin and are functions of the vertical coordinate only.

4.3 *Integral formulation for local averages and secondary currents*

It is known that turbulent flows over streamwise ridges of resting particles, observed in the *HP* scenario, typically exhibit secondary currents in the form of counter-rotating cells, a feature referred to as Prandtl's secondary flow of second kind, caused by anisotropy in turbulence (e.g. Bradshaw, 1987). These secondary currents can be quantified with the mean streamwise vorticity:

$$\langle\bar{\omega}_x\rangle = \frac{\partial\langle\bar{w}\rangle}{\partial y} - \frac{\partial\langle\bar{v}\rangle}{\partial z} \tag{12}$$

Typical absolute values for the mean wall-normal and spanwise velocity components reach up to 5% of the bulk velocity (Nezu & Nakagawa, 1993). For geometric and kinematic reasons, secondary cells alternate in sign and have an extent of about H in the wall-normal and spanwise directions, resulting in a spacing of 2 H between ridges. The role of the secondary cells in the flow structure can be investigated employing the DAM framework with local averaging in space, i.e. using the averaging domain of volume $V_{0,2}$ according to Eq. (8). Akin to Eq. (11), the local double-averaged momentum balance for $i = 1$ includes the terms representing the lateral momentum exchange. Based on the analysis presented in Vowinckel, Nikora, et al. (2017), the momentum flux due to spatial correlations (terms 8 and 9) were not included in the analysis due to their small values. Contributions of the interfacial terms 10 and 11 in studying secondary currents were also neglected because the secondary flow predominantly evolves in the flow region above the bed, where no bed particles are present (e.g. Nikora, McLean, et al., 2007). These simplifications allow us to make the following approximation for the steady flow case (i.e. the time derivative is assumed to be equal to zero):

$$\bar{f}_x\int_y^H \phi_{Vm}\langle\phi_T\rangle\mathrm{d}y^* = \int_y^H\left[\frac{\partial\phi_{\text{Vm}}\langle\phi_{\text{T}}\rangle\langle\bar{u}\rangle\langle\bar{v}\rangle}{\partial y^*} + \frac{\partial\phi_{Vm}\langle\phi_T\rangle\langle\bar{u}\rangle\langle\bar{w}\rangle}{\partial z}\right]\mathrm{d}y^*$$
$$+\int_y^H\left[\frac{\partial\phi_{Vm}\langle\phi_T\overline{u'v'}\rangle}{\partial y^*} + \frac{\partial\phi_{Vm}\langle\phi_T\overline{u'w'}\rangle}{\partial z}\right]\mathrm{d}y^*$$
$$+\int_y^H\left[\frac{\partial\phi_{Vm}\langle\phi_T\tilde{\bar{u}}\tilde{\bar{v}}\rangle}{\partial y^*} + \frac{\partial\phi_{Vm}\langle\phi_T\tilde{\bar{u}}\tilde{\bar{w}}\rangle}{\partial z}\right]\mathrm{d}y^* \tag{13}$$

The difference with respect to Eq. (11) is that in Eq. (13) local space averaging following Eq. (8) is used as opposed to the global averaging, Eq. (9), which is employed in Eq. (11). A uniform flow without secondary currents satisfies the conditions $\bar{v} = \bar{w} = 0$ making the streamwise vorticity in Eq. (9) zero. Assuming furthermore statistical homogeneity in the z direction, Eq. (13) reduces to:

$$\bar{f}_x\int_y^H \phi_{Vm}\langle\phi_T\rangle\mathrm{d}y^* = \int_y^H\left[\frac{\partial\phi_{Vm}\langle\phi_T\overline{u'v'}\rangle}{\partial y^*} + \frac{\partial\phi_{Vm}\langle\phi_T\tilde{\bar{u}}\tilde{\bar{v}}\rangle}{\partial y^*}\right]\mathrm{d}y^* \tag{14}$$

The remaining part of the total shear stress in Eq. (13), hence, can be assigned, at least conceptually, to the stresses induced by secondary currents τ_{sec}. The DAM framework allows evaluating this contribution in a consistent manner and suggests that the following expression can be useful:

$$\frac{\tau_{sec}}{\rho_f} = \int_y^H\left[\frac{\partial\phi_{Vm}\langle\phi_T\rangle\langle\bar{u}\rangle\langle\bar{v}\rangle}{\partial y^*} + \frac{\partial\phi_{Vm}\langle\phi_T\rangle\langle\bar{u}\rangle\langle\bar{w}\rangle}{\partial z}\right]\mathrm{d}y^*$$
$$+\int_y^H\left[\frac{\partial\phi_{Vm}\langle\phi_T\overline{u'w'}\rangle}{\partial z} + \frac{\partial\phi_{Vm}\langle\phi_T\tilde{\bar{u}}\tilde{\bar{w}}\rangle}{\partial z}\right]\mathrm{d}y^* \tag{15}$$

where the local average is applied; y is an independent variable, τ_{sec} is a function of z and y and thus can be visualized in the x and y plane. Note that the last term on the right-hand-side of Eq. (14) was referred to as the so-called "apparent" stress by Myers (1978) and Shiono and Knight (1991), and is known to be the most important part in Eq. (15).

5 Results

5.1 *Porosities and double-averaged velocities*

The distributions of the key double-averaged quantities, including the bed porosities, are shown in Figs 3–6. These figures are organized as follows. To allow easy comparison, the quantities related to the *HP* scenario are placed on the left-hand side while the results for the *LP* scenario are given on the right-hand side. The spatial distribution of each parameter is displayed as a two-dimensional plot of their locally averaged values with the colour scale always the same for all plots assembled in one figure. Note that the axes are not to scale for theses plots. For technical reasons, the vertical axis was exaggerated by a factor of 2 with respect to the horizontal axis. A one-dimensional plot on the right of each figure represents the global average using $V_{0,1}$.

As discussed in Section 4.1, the total time-space porosity ϕ_{VT} can be presented as the product of the spatial porosity ϕ_{Vm} and

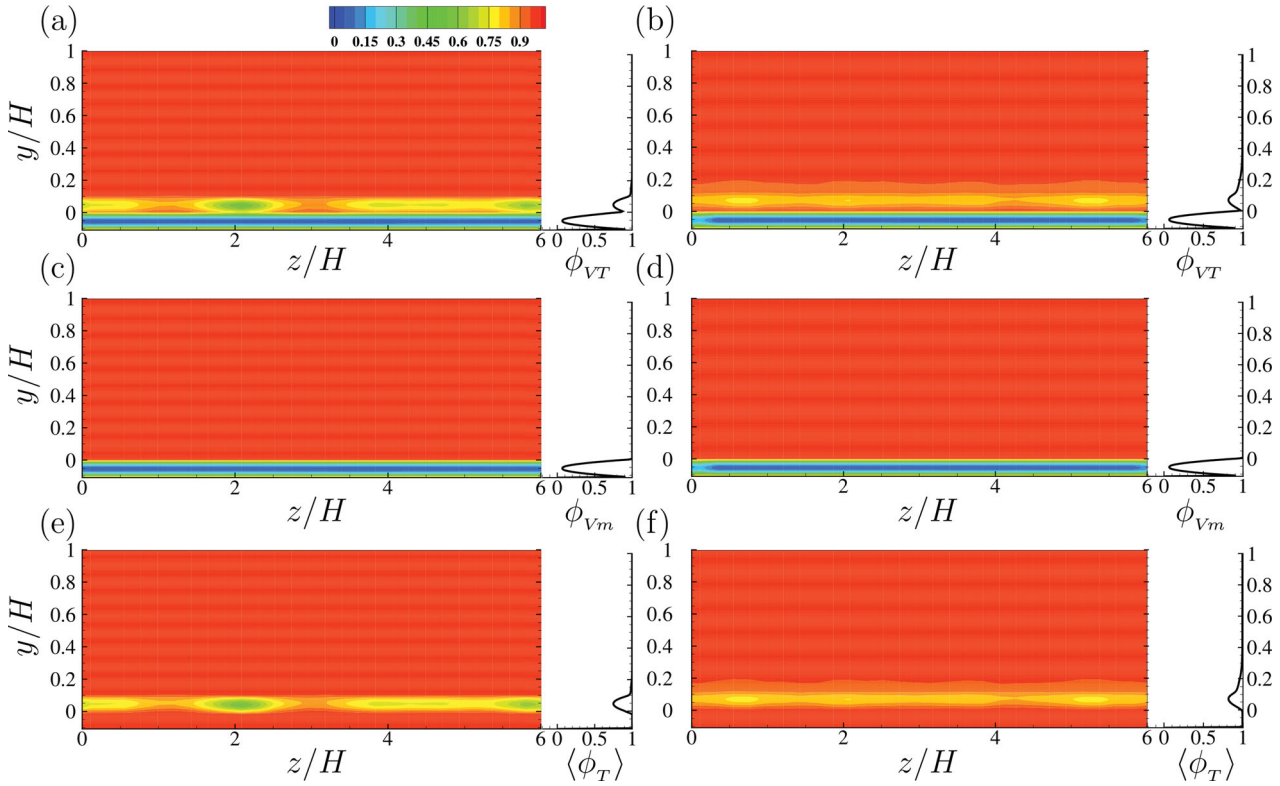

Figure 3 Spatial distribution of the double averaged porosities for the scenarios *HP* (left) and *LP* (right). Contour plots are for local averages and wall-normal profiles are for global averages. (a) Total porosity ϕ_{VT} for scenario *HP*; (b) ϕ_{VT} for scenario *LP*; (c) space porosity ϕ_{Vm} for scenario *HP*; (d) ϕ_{Vm} for scenario *LP*; (e) spatially averaged time porosity $\langle\phi_T\rangle$ for scenario *HP* and (f) $\langle\phi_T\rangle$ for scenario *LP*

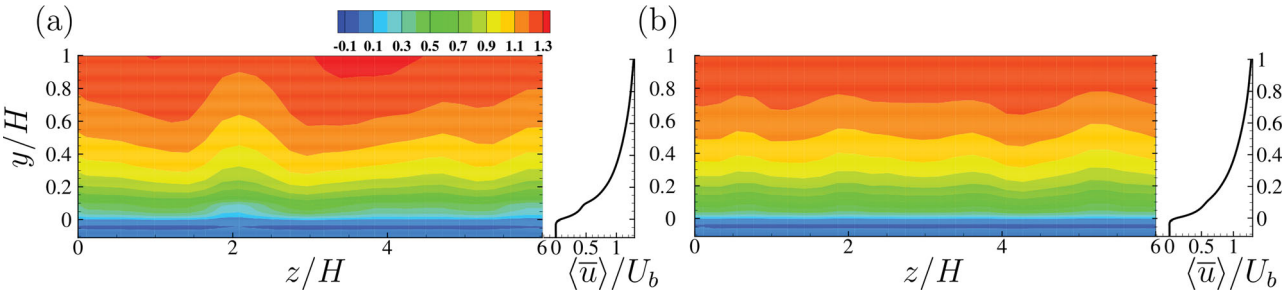

Figure 4 Spatial distribution of the time-space averaged streamwise velocity $\langle\bar{u}\rangle$. (a) Scenario *HP*; (b) scenario *LP*

the spatially averaged temporal porosity $\langle\phi_T\rangle$. In this regard, $(1 - \phi_{VT})$ represents the portion of the averaging domain that has not been visited at all by fluid during the averaging time T_0, while $\langle\phi_T\rangle$ is a measure of the porosity of the mobile granular bed. Figure 3 reveals that for $y > 0$, i.e. above the layer of fixed particles representing the rough wall, $\phi_{Vm} = 1$ for both cases *HP* and *LP*. This stems from the fact that, although the ridges are stable patterns, the individual particles constituting the ridges move, at least from time to time, so that each point above the fixed bed is visited by fluid during the averaging time. Hence, the total porosity of the ridges is equivalent to the spatially averaged temporal porosity $\langle\phi_T\rangle$.

For the case *HP*, the lowest values of the porosity are obtained for the region $0 < y < 0.1H$, in particular at $z/H = 2$, $z/H = 4$, and $z/H = 6$, albeit exhibiting different magnitudes. The ridge at $z/H = 2$ proved to be stable over the entire simulation time. At $z/H = 4$ rather irregular particle forms were observed and a stable pattern with a finite streamwise extent was detected at $z/H = 6$. The particle clusters at $z/H = 4$ and $z/H = 6$ were found to propagate in the streamwise direction with a velocity much smaller than the bulk flow. The one-dimensional profiles of the "global" porosity (Fig. 3a and 3b) exhibit a minimum at the elevation $y = 0.056H = 0.5D$. At the locations $z/H = 2$, 4 and 6, the low porosity, combined with the particle clusters, decelerates the fluid over the whole flow depth and introduces a kink in the globally averaged streamwise fluid velocity profile at $y = 0.11H = 1D$ (Fig. 4a), similarly to the findings of Ferreira, Ferreira, Ricardo, and Franca (2010). The level $y = 0.11H = 1D$ corresponds to the upper crest of mobile particles moving on the fixed bed. The contours of the locally averaged flow velocities (Fig. 4a) reveal that the low momentum fluid is observed at the locations of minimal porosity which are

associated with the particle clusters. Interestingly, Barros and Christensen (2014), who experimentally investigated turbulent flow over an impervious fixed rough bed at a fully rough regime, found transverse flow heterogeneity associated with the transverse heterogeneity in the surface roughness. Our study suggests that the porosity effect is an additional factor explicitly linked to the flow heterogeneity and the occurrence of the secondary flows.

Compared to *HP*, the porosity distribution of the *LP* scenario is much more homogeneous. Nevertheless, four quite regularly spaced maxima of $\langle\phi_T\rangle$ and ϕ_{VT} can be observed at $z/H \approx 0.6$, 2.1, 3.8, and 5.3, which are reflected in the distribution of $\langle\bar{u}\rangle$ displayed in Fig. 4b. The wavelength of this pattern across the flow is 1.5 H and hence shorter compared to scenario *HP*. This is unexpected and could not be easily detected from animations or snapshots shown in Fig. 2. Similar to *HP* (Fig. 4a), velocity contours in Fig. 4b reveal transverse flow heterogeneity associated with the heterogeneity in bed porosity (Fig. 3). It is important to note that bed roughness effects are not as profound here as in the *HP* case, thus strengthening our suggestion above about the potential importance of the porosity effects in generating secondary currents.

5.2 *Momentum fluxes*

In the following, the momentum fluxes due to the turbulent and the form-induced fluctuations, normalized by the fluid density, are presented in Figs 5 and 6. Although all flux components were explored, only the most prominent ones are reported here. Among them, the streamwise turbulent flux $\langle\overline{u'u'}\rangle$ is largest,

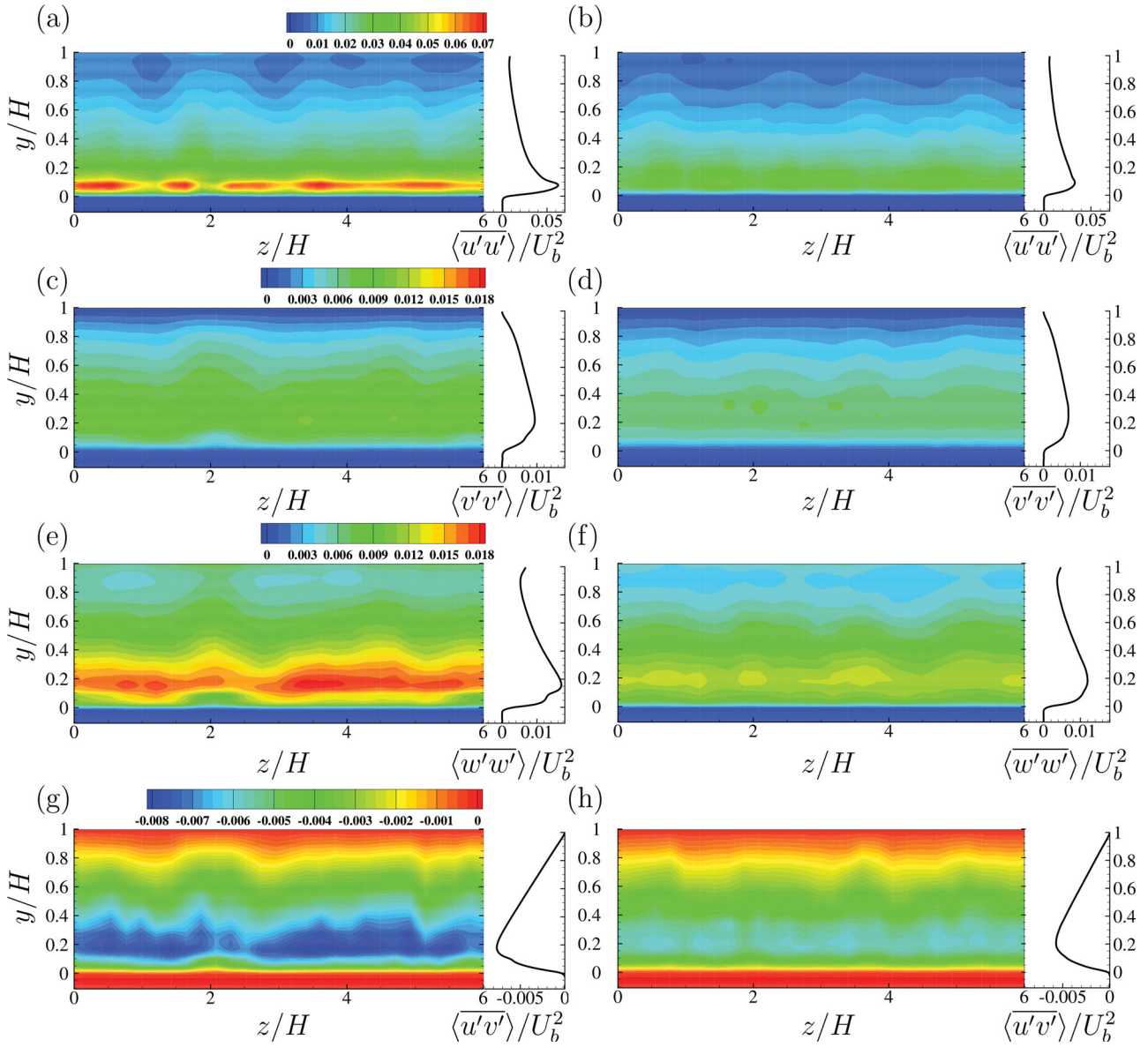

Figure 5 Spatial distribution of the time-space averaged turbulent momentum fluxes. (a) Streamwise flux $\langle\overline{u'u'}\rangle/U_b^2$ for scenario *HP*; (b) streamwise flux $\langle\overline{u'u'}\rangle/U_b^2$ for scenario *LP*; (c) wall-normal flux $\langle\overline{v'v'}\rangle/U_b^2$ for scenario *HP*; (d) wall-normal flux $\langle\overline{v'v'}\rangle/U_b^2$ for scenario *LP*; (e) spanwise flux $\langle\overline{w'w'}\rangle/U_b^2$ for scenario *HP*; (f) spanwise flux $\langle\overline{w'w'}\rangle/U_b^2$ for scenario *LP*; (g) shear stress $\langle\overline{u'v'}\rangle/U_b^2$ for scenario *HP*; (h) shear stress $\langle\overline{u'v'}\rangle/U_b^2$ for scenario *LP*

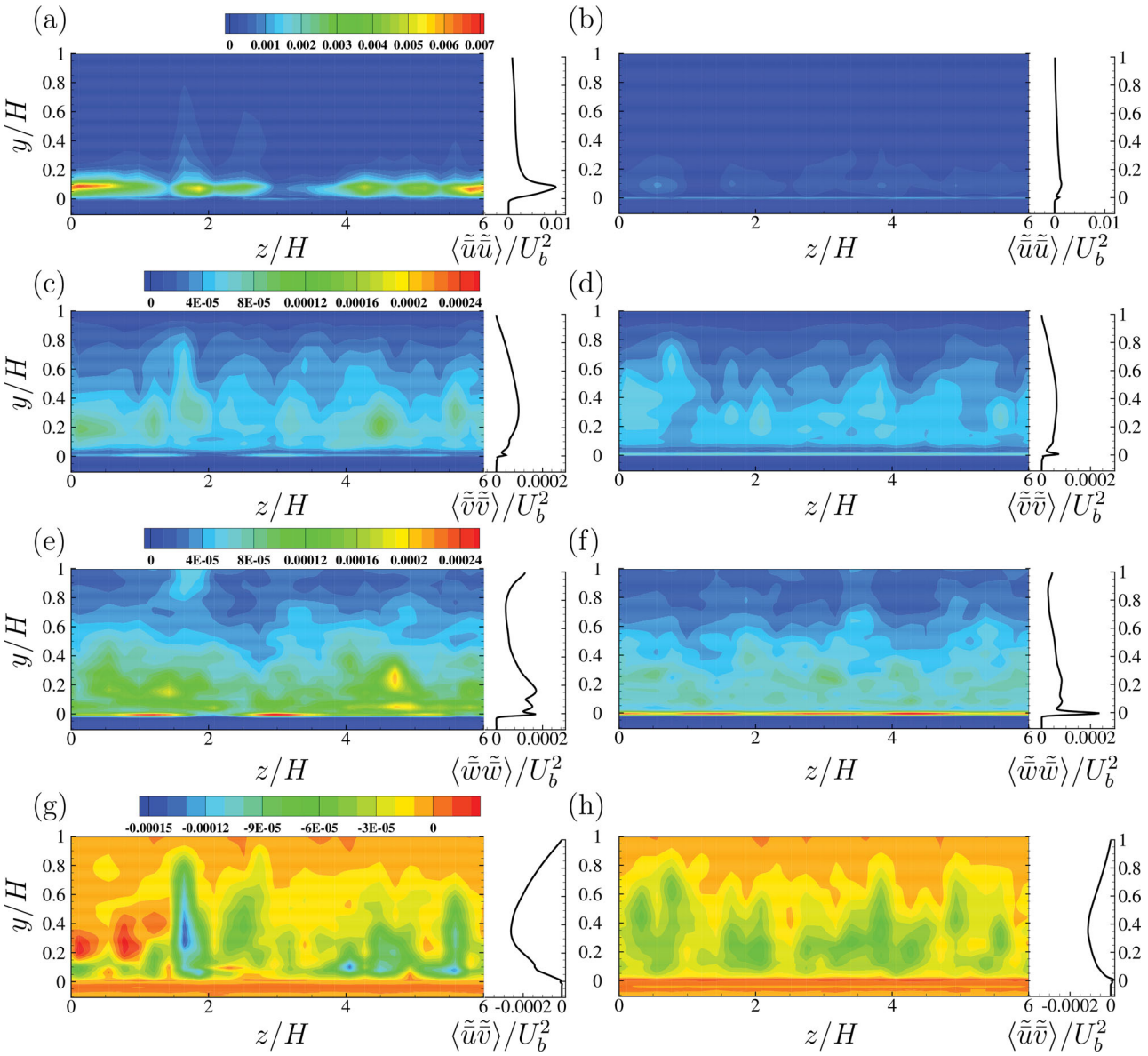

Figure 6 Spatial distribution of form-induced momentum fluxes. (a) Streamwise flux $\langle\tilde{\tilde{u}}\tilde{\tilde{u}}\rangle/U_b^2$ for scenario *HP*; (b) streamwise flux $\langle\tilde{\tilde{u}}\tilde{\tilde{u}}\rangle/U_b^2$ for scenario *LP*; (c) wall-normal flux $\langle\tilde{\tilde{v}}\tilde{\tilde{v}}\rangle/U_b^2$ for scenario *HP*; (d) wall-normal flux $\langle\tilde{\tilde{v}}\tilde{\tilde{v}}\rangle/U_b^2$ for scenario *LP*; (e) spanwise flux $\langle\tilde{\tilde{w}}\tilde{\tilde{w}}\rangle/U_b^2$ for scenario *HP*; (f) spanwise flux $\langle\tilde{\tilde{w}}\tilde{\tilde{w}}\rangle/U_b^2$ for scenario *LP*; (g) shear stress $\langle\tilde{\tilde{u}}\tilde{\tilde{v}}\rangle/U_b^2$ for scenario *HP*; (h) shear stress $\langle\tilde{\tilde{u}}\tilde{\tilde{v}}\rangle/U_b^2$ for scenario *LP*

compared to the wall-normal flux $\langle\overline{v'v'}\rangle$ and the spanwise flux $\langle\overline{w'w'}\rangle$ (Fig. 5). Close to the free surface, the data support a conjecture that the kinetic energy is transferred from the *v*-component to the two horizontal velocity components (Nezu & Nakagawa, 1993).

Starting with scenario *HP*, it is noticed that $\langle\overline{u'u'}\rangle$ exhibits maxima on both sides of the ridges. This is visible at $y \approx 0.07\ H$ and even much higher above, where the distortions of the contour lines are significant (Fig. 5a). It is also visible that the presence of particles, i.e. a low porosity, hampers the local turbulent fluxes in the near wall region at $z/H = 2$. This is especially true for $\langle\overline{w'w'}\rangle$ (Fig. 5e). The global average of the Reynolds shear stress $\langle\overline{u'v'}\rangle$ displayed in the one-dimensional profiles of Fig. 5g peaks directly above the layer of mobile particles at $y \approx 1.5\ D = 0.167H$ and becomes zero close to and within the fixed bed for both local and the global averages. There is also a kink at $y \approx 1D = 0.11H$ in the one-dimensional profiles of $\langle\overline{w'w'}\rangle$ and $\langle\overline{u'v'}\rangle$. At this level, the cluster particles develop another local boundary layer with high viscous and turbulent shear stresses. Similar observations were made in the experimental work of Ferreira et al. (2010).

The results for the *HP* case are now compared to those of the *LP* case. Although the number of mobile particles introduced is the same in both scenarios, the normalized turbulent fluxes shown in the right-hand plots of Fig. 5 differ quantitatively from those in the *HP* case. Indeed, the magnitudes of the globally-averaged turbulent fluxes in the *LP* case are smaller by up to 50%. This is due to the fact that the momentum exchange of the light particles with the rough bottom by collisions and contacts is weaker, resulting in a lower relative particle velocity.

The effect of loss of kinetic energy due to collisions can be quantified by the particle Reynolds number R_p based on the "global" slip velocity ($\langle\bar{u}_p\rangle - \langle\bar{u}\rangle$), which reaches values of up to 110 for the *HP* case, while this quantity remains as low as $\mathsf{R}_p = 40$ for the *LP* case (Vowinckel & Fröhlich, 2012). For scenario *LP*, the spatial distribution of the locally averaged turbulent fluxes is noticeably more homogeneous, and the one-dimensional global profiles do not show the distinct kinks reported for $\langle\overline{w'w'}\rangle$ and $\langle\overline{u'v'}\rangle$ in the *HP* scenario. Slight distortions in the level lines of $\langle\overline{u'u'}\rangle$ are visible though and localized near the points where $\langle\phi_T\rangle$ locally has larger values at the bottom (Fig. 3).

The locally averaged form-induced momentum fluxes $\langle\tilde{\bar{u}}\tilde{\bar{u}}\rangle$ illustrate the effects of heterogeneity of the particle distribution for both scenarios. For the *HP* case, the streamwise flux $\langle\tilde{\bar{u}}\tilde{\bar{u}}\rangle$ shows fairly large values in the near-wall region (Fig. 6a), which are of the same order of magnitude as reported for the turbulent momentum fluxes $\langle\overline{u'u'}\rangle$. In the outer flow, $\langle\tilde{\bar{u}}\tilde{\bar{u}}\rangle$ becomes negligibly small. Compared to the maximum of $\langle\tilde{\bar{u}}\tilde{\bar{u}}\rangle$, the other two normal form-induced stresses, $\langle\tilde{\bar{v}}\tilde{\bar{v}}\rangle$ and $\langle\tilde{\bar{w}}\tilde{\bar{w}}\rangle$, are two orders of magnitude smaller (Fig. 6c and 6e). The locally averaged form-induced shear stress $\langle\tilde{\bar{u}}\tilde{\bar{v}}\rangle$ of the *HP* case, displayed in Fig. 6g, is mostly negative and exhibits some variability in vertical and spanwise directions. This pattern indicates the existence of at least two counter-rotating secondary current cells with upward fluid motion at approximately $z/H \approx 2$ and downward motions of $z/H \approx 1.5$ and $z/H \approx 2.5$, albeit with different magnitude. Indeed, a high "hill" in the contour plot of $\langle\tilde{\bar{u}}\tilde{\bar{v}}\rangle$ at $z/H \approx 2$, superimposed with a "valley" in the contour lines of $\langle\bar{u}\rangle$ in Fig. 4a, suggests upward motions. An opposite picture is observed in the regions surrounding the locations at $z/H \approx 1.5$ and $z/H \approx 2.5$, where hills of the $\langle\bar{u}\rangle$ distribution coincide with the troughs of the $\langle\tilde{\bar{u}}\tilde{\bar{v}}\rangle$ distribution, consistent with the downward fluid motions. A similar pattern is also observed in the vicinity of $z/H \approx 6$. At both $z/H \approx 2$ and $z/H \approx 6$, the upward motions are associated with ridge crests clearly visible in Fig. 6. The globally-averaged values of $\langle\tilde{\bar{u}}\tilde{\bar{v}}\rangle$ appear to be nearly two times larger than their locally-averaged values. This discrepancy should not be surprising as the global averaging accounts for ridge-scale variability, which is much higher compared to the particle-scale variability that dominates locally-averaged quantities such as $\langle\tilde{\bar{u}}\tilde{\bar{v}}\rangle$.

For the *LP* case, all three locally-averaged normal form-induced stresses, i.e. $\langle\tilde{\bar{u}}\tilde{\bar{u}}\rangle$, $\langle\tilde{\bar{v}}\tilde{\bar{v}}\rangle$ and $\langle\tilde{\bar{w}}\tilde{\bar{w}}\rangle$, are smaller compared to their counterparts in the case *HP* while their spatial distribution is much less heterogeneous (Fig. 6). The global averages of $\langle\tilde{\bar{u}}\tilde{\bar{u}}\rangle$, $\langle\tilde{\bar{v}}\tilde{\bar{v}}\rangle$ and $\langle\tilde{\bar{w}}\tilde{\bar{w}}\rangle$ are also different, with the most notable feature being a sharp peak at the top of the fixed-bed particles in the $\langle\tilde{\bar{w}}\tilde{\bar{w}}\rangle$ distribution. The absence of such a distinct peak in the *HP* case reflects "smoothing" effects of bed ridges in the averaging process, making the near-bed peak much wider and spreading it over a layer from $y/H \approx 0$ to $y/H \approx 0.2$. The data obtained convincingly show that the form-induced stresses in flows over mobile granular-beds may substantially contribute to the overall momentum flux. Furthermore, the comparison of the present mobile-bed simulation data with clear-water laboratory data of Cameron et al. (2008), collected at nearly the same background conditions, shows that although the maximum magnitudes of $\langle\tilde{\bar{u}}\tilde{\bar{u}}\rangle$ and $\langle\tilde{\bar{v}}\tilde{\bar{v}}\rangle$ in clear-water case are similar to the mobile-bed values in the simulations, their vertical distributions are distinctly different. In the clear-water case the values of $\langle\tilde{\bar{u}}\tilde{\bar{u}}\rangle$ and $\langle\tilde{\bar{v}}\tilde{\bar{v}}\rangle$ attain maxima at the particle tops and then sharply reduce to zero within a very thin layer from $y/H \approx 0$ to $y/H \approx 0.04$. The distribution and magnitude of the shear stress $\langle\tilde{\bar{u}}\tilde{\bar{v}}\rangle$ in the clear-water case is also markedly different: $\langle\tilde{\bar{u}}\tilde{\bar{v}}\rangle$ is positive, not negative as in the present mobile-bed case. It attains a maximum at the bed particle tops and is non-zero only within a very narrow layer from $y/H \approx 0$ to $y/H \approx 0.02$. Clearly, the bed mobility and bed structure significantly modify the distribution of all stresses $\langle\tilde{\bar{u}}_i\tilde{\bar{u}}_j\rangle$, making it more influential compared to the clear-water case. This comparison advocates the urgency of collecting data on $\langle\tilde{\bar{u}}_i\tilde{\bar{u}}_j\rangle$ for a wide range of background conditions and different bed roughness to create a basis for mechanism-based parameterizations of form-induced stresses, which is currently absent. More details on time-averaged and globally-averaged turbulent quantities for the studied background conditions and clear-water case can be found in Cameron et al. (2008) and Vowinckel et al. (2012, 2014).

5.3 *Bulk momentum balance and bed resistance*

This section investigates the "globally" averaged momentum balance expressed by Eq. (11), to make a comparison between the different momentum fluxes in terms of their significance for the double-averaged momentum balance of Eq. (10). In Nikora, McEwan, et al. (2007) it was argued that only the terms 3, 5, 6, 10 and 11 are significant for fixed-bed uniform turbulent flows with high submergences, while the terms 2 and 7 can be neglected (terms 8 and 9 vanish for fixed-bed flows). For the case of a mobile granular bed, this assumption does not necessarily hold, since particles are free to move and may activate momentum fluxes in the wall-normal direction that are negligible in the fixed-bed flows. Hence, all balance terms are accounted for in the present analysis to fully explore the importance of the different terms of Eq. (11). A direct evaluation of the interfacial terms 10 and 11 is not possible by construction of the numerical method (Kempe & Fröhlich, 2012a). However, since the total momentum balance must add up to zero, the sum of the evaluated terms must be equal to the sum of the "out-of-balance" terms comprising the local acceleration (term 1) and the two interfacial terms 10 and 11.

Figure 7 highlights the importance of the different terms of the integral momentum balance wrapping-up the outcomes of Section 5.2. The most dominant contribution to the total stress originates from the turbulent fluctuations (term 5). This finding is consistent with the results of Shao, Wu, and Yu (2012) and Vowinckel et al. (2012, 2014) that turbulent stresses are amplified by the introduction of particles substantially heavier than the fluid and much larger than the viscous length scales.

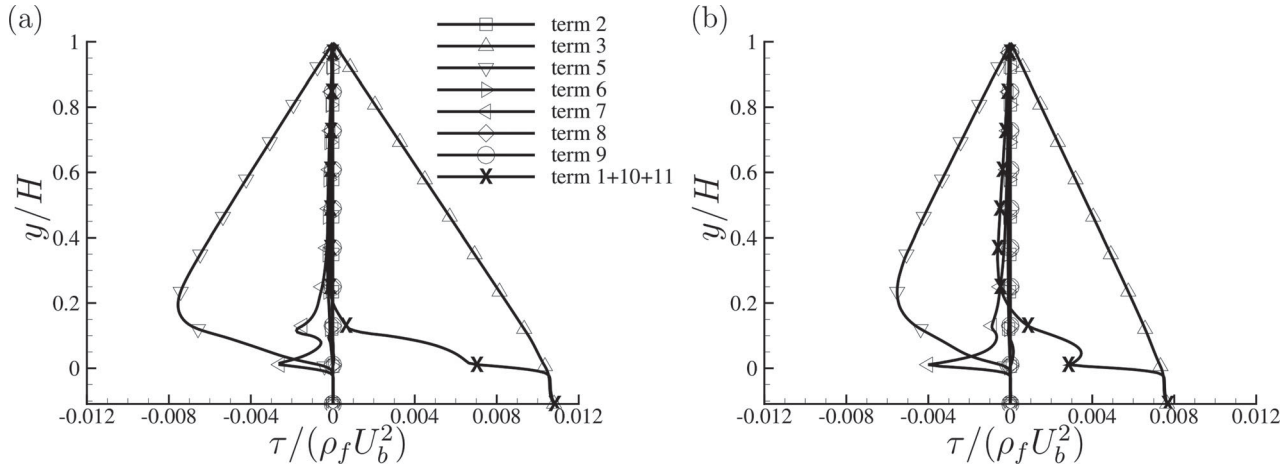

Figure 7 Wall-normal distribution of the different terms of the integral form of the momentum balance Eq. (11). (a) Scenario *HP*; (b) scenario *LP*. Vertical distances between symbols are equal to *D*. Note that the sum of terms 1, 10, and 11 are shown with negative sign for clarity

Although it is noted in Section 5.2 that the form-induced momentum fluxes (term 6 in Eq. 11) can contribute to the momentum balance locally in the near-wall region, their contribution remains small if global averaging is considered. In the present case, the local acceleration (term 1 in Eq. 11) is close to zero as the averaging time is very long, so that the out-of-balance quantity should be equal to the drag terms 10 and 11, thus representing the sink of momentum taken up by the mobile and fixed bed particles. These two terms vanish in the outer flow where no particles are present. Indeed, it is observed that the other terms in Eq. (11) add up to zero in that region, thus demonstrating that sufficient data were gathered to reach appropriate statistical convergence. The computed sum of terms 10 and 11 has two distinct kinks at $y = 0$ and $y = 0.11H = 1D$ (Fig. 7). As expected, the mobile particles of scenario *HP*, located mainly within $0 < y < 0.1H$, take up the gross part of the momentum supplied by the driving volume force (term 3), whereas for scenario *LP* the strongest gradient of the drag terms is observed for the interval $-0.05H < y < 0$, i.e. within the interstitial spaces of the fixed granular bed.

Bearing in mind that at $y = 0$ and $y = H$ terms 1, 2, 5, 6, 8, and 9 in Eq. (11) become negligible due to the boundary conditions, Eq. (11) can be integrated to obtain:

$$\begin{aligned}\bar{f}_x \int_0^H \phi_{Vm}\langle\phi_T\rangle \mathrm{d}y^* &= \int_0^{\mathrm{H}} \frac{1}{V_0} \overline{\iint_{S_{int}} \left(\nu_f \frac{\partial u_i}{\partial x_j}\right) n_y \mathrm{d}S}^{s} \mathrm{d}y^* \\ &\quad - \int_0^H \frac{1}{\rho_f}\frac{1}{V_0} \overline{\iint_{S_{int}} p n_x \mathrm{d}S}^{s} \mathrm{d}y^* - \phi_{Vm}\left\langle \phi_T \nu_f \overline{\frac{\partial u}{\partial y}} \right\rangle\Big|_{y=0}\end{aligned} \tag{16}$$

The terms on the right-hand side of Eq. (16) determine the bed resistance, i.e. the total wall stress, and are balanced by the momentum supply. As mentioned above, the direct computation of the right-hand side of Eq. (16) is not possible with the present data, but the evaluation of the left-hand side of this equation is possible and can be used to define a wall shear stress $\tau_w^{(p)}$ as:

$$\frac{\tau_w^{(p)}(\Lambda)}{\rho_f} = \bar{f}_x \int_0^H \phi_{Vm}\langle\phi_T\rangle \mathrm{d}y^* \tag{17}$$

where (p) indicates *a posteriori* values. This quantity represents the bed-shear stress, spatially averaged over a horizontal plane area $\Lambda = [0; L_x] \times [0; L_z]$, where the argument Λ is used to distinguish it from locally averaged values. This quantity is induced by the bottom wall, the fixed particles, and the moving granular bed and yields the total stress taken up by the complex phase boundary in a straightforward manner. From the analysis conducted here, an *a posteriori* friction velocity $u_\tau^{(p)} = \sqrt{\tau_w^{(p)}/\rho_f}$ of the particle-laden flow can be determined and used to define the relevant dimensionless *a posteriori* quantities of the flow with bed-load transport, which are collected in Table 1. The dimensionless numbers $\tau_w^{(p)}/(\rho_f U_b^2)$ and $u_\tau^{(p)}/U_b$ in Table 1 give an integral measure of the total hydraulic resistance introduced by the mobile bed. While the particle Reynolds number D^+ for the unladen rough-bed scenario is 19.2 (Vowinckel, Nikora, et al., 2017), it is increased to $\mathsf{D}^{+(\mathrm{p})} = 30.7$ in scenario *HP*. Hence, increasing the amount of mobile particles by 30% of one layer of fixed spheres yields an increase of the bed shear stress by 60% (i.e. $\mathsf{D}^{+(\mathrm{p})}/\mathsf{D}^+ = 1.60$). This shows that the patterns of mobile particles described in Section 3 act as factors substantially enhancing the hydraulic resistance of the bed. For scenario *LP* with the same number of mobile particles (but lighter), the particle Reynolds number is $\mathsf{D}^{+(\mathrm{p})} = 25.8$, which

Table 1 *A posteriori* dimensionless numbers for the present mobile bed conditions

Scenario	$\tau_w^{(p)}/(\rho_f U_b^2)$	$u_\tau^{(\mathrm{p})}/U_b$	$\mathsf{D}^{+(\mathrm{p})}$	$\mathsf{R}_\tau^{(\mathrm{p})}$
HP	1.05×10^{-2}	0.102	30.7	276
LP	0.74×10^{-2}	0.086	25.8	233

is 34% larger than the corresponding value for the unladen flow (i.e. $\mathsf{D}^{+(p)}/\mathsf{D}^{+} = 1.34$). Hence, the increase in the shear stress in the *HP* case is almost equivalent to the increase of the interface area S_{int} between the particles and the fluid.

It is important to highlight that *a posteriori* value of $\mathsf{D}^{+(p)}$ does not provide a suitable measure of the actual resolution of the DNS. Indeed, it was reported by Uhlmann (2008) that a discretization at $D/\Delta_x = 20$ is sufficient to simulate particle Reynolds numbers (based on the slip velocity) with values of up to 136 (slip velocity here is the difference between the particle velocity and mean fluid velocity). The value of 136 is well above the present Reynolds number as demonstrated in Vowinckel and Fröhlich (2012) so that even when based on $\mathsf{D}^{+(p)}$, the spatial resolution by the present grid is sufficiently fine to warrant a true DNS.

Finally, note that computing a modified *a posteriori* Shields number is not appropriate, as the concept of Shields (1936) applies to the threshold of mobilization and not to the situation of a sizable amount of sediment being transported. It furthermore assumes uniform roughness, which is no longer the case with non-uniform distribution of particles accumulating in clusters, such as the ridges encountered in scenario *HP*.

5.4 *Secondary currents*

As outlined in Section 4.3, secondary currents are often induced by turbulence anisotropy and show a typical cellular pattern with a wavelength of 2 *H*. Indeed, these features can be observed for scenario *HP* when considering the spatial distribution of the locally averaged turbulent momentum flux as well as the form-induced momentum flux (Figs 5 and 6). The effects of secondary currents in the *HP* case have already been briefly discussed in Section 5.2. Here, further details are provided. Taking the advantage of DAM as outlined in Section 4.3, the stress τ_{sec}, induced by secondary currents and defined by Eq. (15), is computed and its spatial distribution is illustrated in Fig. 8 for both simulation scenarios. Note that for technical reasons the vertical axis was exaggerated by a factor of 2 with respect to the horizontal axis.

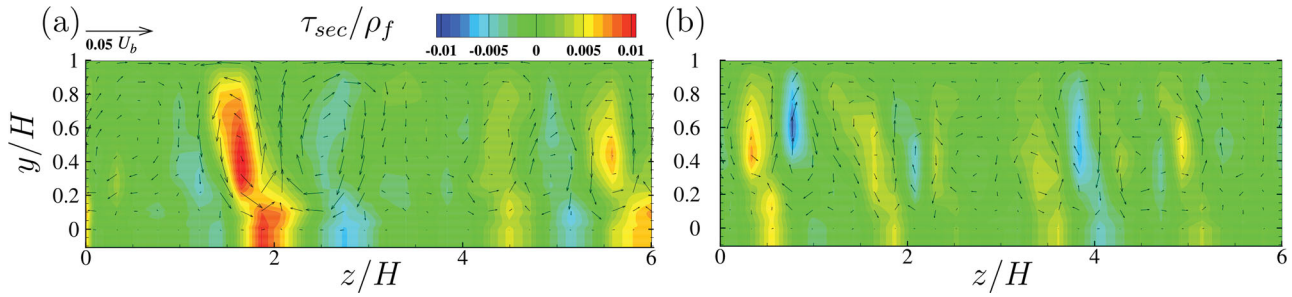

Figure 8 Secondary currents represented by vectors $(w_{sec}, v_{sec})^T$, and spatial distribution of τ_{sec} for (a) scenario *HP* and (b) scenario *LP*. The magnitude of the reference vector is 0.05 U_b. Note that horizontal and vertical axes are not to scale

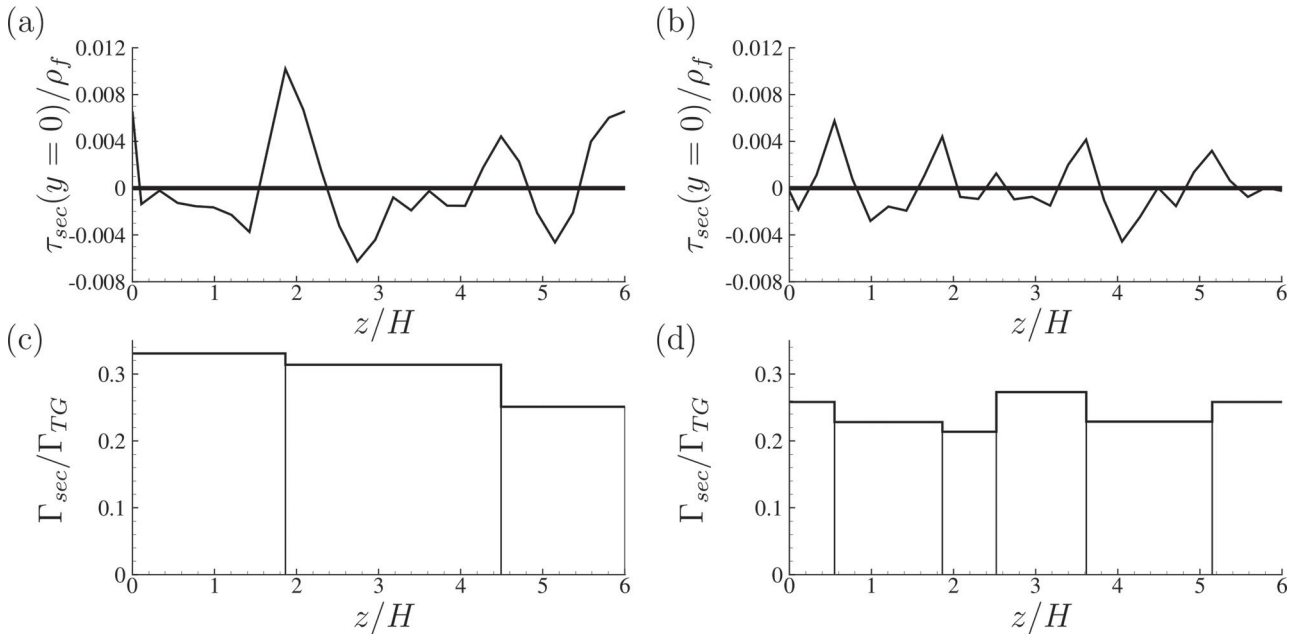

Figure 9 Stress induced by secondary currents in the near-wall region. (a) Scenario *HP* and (b) scenario *LP*. Integrated vorticity Γ_{sec} for different cells of secondary current normalized by the vorticity of a Taylor–Green vortex Γ_{TG}. (c) Scenario *HP* and (d) scenario *LP*

The plots in Fig. 8 also provide vectors of the mean secondary flow components, which are defined as:

$$v_{sec} = \langle \bar{v} \rangle_{V_{0,2}} - \langle \bar{v} \rangle_{V_{0,1}} \tag{18a}$$

$$w_{sec} = \langle \bar{w} \rangle_{V_{0,2}} - \langle \bar{w} \rangle_{V_{0,1}} \tag{18b}$$

with the local averaging volume denoted by the subscript $V_{0,2}$ and the global averaging volume by $V_{0,1}$.

As expected, the vector plots in Fig. 8 reveal several cells with alternating up-welling and down-welling motions clearly visible in the y–z plane. These patterns extend over the entire flow depth and indicate regions of secondary currents with different magnitude. In the outer flow, τ_{sec} is large where strong gradients in the spanwise direction for the terms involved in Eq. (15) are observed, for example in the centre of the vortex at $z \approx 1.5H$. In the near-wall region at $y \approx 0$, on the other hand, strong positive stresses in the near-wall region correspond to the upward fluid motion and vice versa.

The cells of the secondary currents are further analysed in a quantitative way assessing their spatial extent as well as the magnitude. To define the spanwise extent, cuts of the secondary stress in the near-wall region are plotted in Fig. 9a and 9b. The spanwise extent of a couple of counter-rotating cells of secondary flow can now be assessed as the interval between two local maxima with $\tau_{sec} > 0$. One may note that the peaks in Fig. 9a and 9b correspond to the minima of the porosity in the near-wall region reported in Fig. 3. For scenario *HP*, three cells can be identified with an average spacing of $2H$. The strongest peaks are at $z = 0$ and $z = 2H$, with the latter also being the position of the stable ridge. In addition, two more pairs of counter-rotating cells are located in the intervals $2H \leq z \leq 4.5H$ and $4.5H \leq z \leq 6H$. For the *LP* scenario with light particles, five cells are observed indicated by the peaks of $\tau_{sec}(y = 0)$. For this scenario, the coupled cells have smaller values of $\tau_{sec}(y = 0)$ and a smaller spanwise extent of $\approx 1.3H$.

The magnitude of the secondary flow can be assessed by computing a vorticity, averaged over the full wall-normal extent and spanwise stretch of the coupled cell:

$$\Gamma_{sec} = \frac{1}{U_b(z_{0,n+1} - z_{0,n})} \int_0^H \int_{z_{0,n}}^{z_{0,n+1}} |\langle \bar{\omega} \rangle_x| \mathrm{d}z \, \mathrm{d}y \tag{19}$$

where $z_{0,n}$ is the spanwise coordinate of the nth peak reported in Fig. 9a and 9b. To provide a reference, this averaged vorticity is normalized by the vorticity of the initial condition of a two-dimensional Taylor–Green vortex. The parameters for this artificial reference were chosen in accordance with idealized parameters of a coupled cell of secondary flow given by Nezu and Nakagawa (1993), i.e. the typical wavelength and the maximal velocity were set to $\lambda_z = 2H$ and $\sqrt{v_{sec}^2 + w_{sec}^2} = 0.05 U_b$, respectively. This yields the following analytical expressions of the velocity components for the prototype vortex:

$$v_{TG} = 0.05\, U_b \cos(2\pi z/\lambda_z)\, \sin(\pi y/H) \tag{20a}$$

and

$$w_{TG} = -0.05\, U_b \sin(2\pi z/\lambda_z)\, \cos(\pi y/H) \tag{20b}$$

for the wall-normal and the spanwise vector components, respectively. Then, the vorticity of the prototype vortex was computed using Eqs (20a) and (20b), and in turn was used to obtain Γ_{TG} via Eq. (19). The averaged relative vorticity is plotted in Fig. 9c and 9d. As expected, all identified coupled cells have a lower vorticity than the prototype vortex. This can be associated with different boundary conditions. While a free-slip condition is assumed for the prototype vortex, particles introduce a "no-slip" condition on the bottom of the channel which slows down the fluid in the near-wall region. Nevertheless, for scenario *HP* the identified cells have a vorticity between 25% and 33% of the modelled prototype vortex (Fig. 9c). These cells with the highest magnitude at $0 \leq z \leq 2H$ have their edges at the large scale cluster of slowly moving particles at $z = 0$ and the stable ridge at $z = 2\ H$. The cells at $2H \leq z \leq 4.5H$ having a similar magnitude in Γ_{sec} also terminate at the stable ridge. The boundaries of the third couple of cells in the interval $4.5H \leq z \leq 6H$ are not as distinct, which leads to a decreased vorticity. The light particles of scenario *LP* induce weaker secondary currents with values between 23% and 26% of the modelled prototype vortex (Fig. 9d).

For the simulations presented, the obtained results illustrate that not only do the particles accumulate in low-speed streaks, as it has been suggested by some experimental work (Niño & Garcia, 1996) and numerical studies with point particles transported over smooth walls (e.g. Marchioli & Soldati, 2002; Vreman, 2007) and wavy beds (e.g. Milici, De Marchis, Sardina, & Napoli, 2014), and in simulations with particles of finite size (Kidanemariam, Chan-Braun, Doychev, & Uhlmann, 2013), but the particle–fluid interactions significantly reorganize the flow. In the present case, large-scale vortical cells emerged adjusting and enhancing the spanwise heterogeneities to reach a new state of equilibrium for the given bulk physical conditions. These persistent cells of secondary currents develop due to the introduction of particles heavier than the fluid that form particle clusters moving in the streamwise direction and having time scales much larger than the turbulence time scales. Lighter particles that are fully mobilized significantly weaken this pattern (as in our *LP* case).

6 Conclusions

Highly resolved direct numerical simulations of a turbulent open channel flow laden with monodisperse spherical particles

were performed. Two simulation scenarios with two distinctly different transport modes, partially and fully mobilized, were compared to investigate the modes of sediment transport and associated flow features. The application of the DAM allowed the flow to be analysed in a systematic way addressing several typical length scales of the flow spanning from the grain scale to large-scale secondary currents to the entire computational domain. This was done on the basis of a set of physically meaningful double-averaged quantities like turbulent and form-induced momentum fluxes as well as boundary stresses. The results highlight the importance of form-induced fluxes whenever averaging in flows over a heterogeneous terrain is performed. It is demonstrated that mobile particles have the capability to take up the gross part of the stresses induced by the momentum supply. This yields an increase in hydraulic resistance and the formation of cells of secondary currents rearranging the mean flow field of the entire channel. The present paper will hopefully guide follow-up studies to exploit the advantages of the DAM, eventually opening up the possibility to model the additional fluxes introduced by the mobile granular bed.

Acknowledgements

The authors gratefully acknowledge the Centre for Information Services and High Performance Computing (ZIH), Dresden, and the Jülich Supercomputing Centre (JSC) for providing computing time. The authors thank Markus Uhlmann and Clemens Chan-Braun for stimulating discussions on bed-load transport.

Funding

The present work was funded by the German Research Foundation (DFG) via the project [FR 1593/5-2] and was partly supported by the Engineering and Physical Sciences Research Council (EPSRC) UK, Grant [EP/G056404/1].

Notation

D = particle diameter (m)
D^+ = particle Reynolds number (–)
$\mathbf{f} = (f_x, f_y, f_z)^T$ = driving volume force (m s^{-2})
$\mathbf{f}_{IBM}$ = IBM source term (m s^{-2})
H = channel height (m)
$\mathbf{I}$ = identity matrix (–)
L_x, L_y, L_z = extent in streamwise, wall-normal, and spanwise direction (m)
$\mathbf{n}$ = outward-pointing normal vector (–)
p = pressure (kg m^{-1} s^{-2})
R_b = bulk Reynolds number (–)
R_p = particle Reynolds number (–)
R_τ = frictional Reynolds number (–)
Sh = Shields parameter (–)
$\mathsf{Sh}_{\mathrm{crit}}$ = critical Shields parameter (–)
T_0 = total averaging time (s)
T_b = bulk time unit (s)
T_f = time during which a given location is occupied by fluid (s)
U_b = bulk velocity (m s^{-1})
$\mathbf{u} = (u_1, u_2, u_3)^T = (u, v, w)^T$ = fluid velocity vector (m s^{-1})
$\mathbf{u}_p$ = particle velocity vector (m s^{-1})
u_τ = friction velocity (m s^{-1})
V_0 = total volume of the averaging domain (m^3)
$V_{0,1}$ = global averaging domain (m^3)
$V_{0,2}$ = local averaging domain (m^3)
V_m = volume within V_0 occupied by fluid (m^3)
v_{sec} = wall-normal component of the mean secondary flow (m s^{-1})
v_{TG} = wall-normal component of an ideal initial Taylor–Green vortex (m s^{-1})
w_{sec} = spanwise component of the mean secondary flow (m s^{-1})
w_{TG} = spanwise component of an ideal initial Taylor Green vortex (m s^{-1})
$\mathbf{x} = (x_1, x_2, x_3)^T = (x, y, z)^T$ = position vector (m)
$\Delta_x, \Delta_y, \Delta_z$ = grid cell size in streamwise, wall-normal, and spanwise direction (m)
Γ_{sec} = mean vorticity normalized over a cell of secondary current (–)
Γ_{TG} = Taylor–Green-based vorticity (–)
γ = clipping function (–)
θ = scalar fluid quantity (–)
$\bar{\theta}$ = time averaged quantity (–)
θ = space averaged quantity (–)
$\bar{\theta}$ = spatial deviation of a double-averaged quantity (–)
$\theta^{(p)}$ = a posteriori scalar fluid quantity (–)
Λ = horizontal plane (m^2)
λ_z = typical spanwise wavelength
ν_f = kinematic viscosity (m^2 s^{-1})
ρ_f = fluid density (kg m^{-3})
ρ_p = particle density (kg m^{-3})
τ_{sec} = stresses induced by secondary currents (kg m^{-1} s^{-2})
τ_w = wall shear stress (kg m^{-1} s^{-2})
ϕ_T = time porosity (–)
ϕ_{Vm} = space porosity (–)
ϕ_{VT} = total porosity (–)
Ω = computational domain (m)
ω_x = streamwise vorticity (s^{-1})

References

Allen, J. R. L. (1982). *Sedimentary structures, their character and physical basis* (Vol. *1*). Amsterdam: Elsevier.

Ancey, C., & Heyman, J. (2014). A microstructural approach to bed load transport: Mean behaviour and fluctuations of particle transport rates. *Journal of Fluid Mechanics*, *744*, 129–168.

Balachandar, S., & Eaton, J. K. (2010). Turbulent dispersed multiphase flow. *Annual Review of Fluid Mechanics*, *42*, 111–133.

Ballio, F., Nikora, V., & Coleman, S. E. (2014). On the definition of solid discharge in hydro-environment research and applications. *Journal of Hydraulic Research*, *52*(2), 173–184.

Barros, J. M., & Christensen, K. T. (2014). Observations of turbulent secondary flows in a rough-wall boundary layer. *Journal of Fluid Mechanics*, *748*(R1), 1–13.

Bradshaw, P. (1987). Turbulent secondary flows. *Annual Review of Fluid Mechanics*, *19*(1), 53–74.

Cameron, S., Nikora, V., & Coleman, S. (2008). Double-averaged velocity and stress distributions for hydraulically-smooth and transitionally-rough turbulent flows. *Acta Geophysica*, *56*(3), 642–653.

Dey, S. (2014). *Fluvial hydrodynamics*. Heidelberg: Springer.

Ferreira, R. L., Franca, M. J., Leal, J. G. A. B., & Cardoso A. H. (2012). Flow over rough mobile beds: Friction factor and vertical distribution of the longitudinal mean velocity. *Water Resources Research*, *48*(5). doi:10.1029/2011WR011126

Ferreira, R. M., Ferreira, L. M., Ricardo, A. M., & Franca, M. J. (2010). Impacts of sand transport on flow variables and dissolved oxygen in gravel-bed streams suitable for salmonid spawning. *River Research and Applications*, *26*(4), 414–438.

Furbish, D. J., Haff, P. K., Roseberry, J. C., & Schmeeckle, M. W. (2012). A probabilistic description of the bed load sediment flux: 1. Theory. *Journal of Geophysical Research – Earth Surface*, *117*, F03031-1–F03031-21.

Graf, W. (1996). *Hydraulics of sediment transport*. Highlands Ranch, CO: Water Resources.

Gray, W., & Lee, P. C. Y. (1977). On the theorems for local volume averaging of multiphase systems. *International Journal of Multiphase Flow*, *3*(4), 333–340.

Karcz, I. (1966). Secondary currents and the configuration of a natural stream bed. *Journal of Geophysical Research*, *71*(12), 3109–3112.

Kempe, T., & Fröhlich, J. (2012a). An improved immersed boundary method with direct forcing for the simulation of particle laden flows. *Journal of Computational Physics*, *231*(9), 3663–3684.

Kempe, T., & Fröhlich, J. (2012b). Collision modelling for the interface-resolved simulation of spherical particles in viscous fluids. *Journal of Fluid Mechanics*, *709*, 445–489.

Kempe, T., Vowinckel, B., & Fröhlich, J. (2014). On the relevance of collision modeling for interface-resolving simulations of sediment transport in open channel flow. *International Journal of Multiphase Flow*, *58*, 214–235.

Kidanemariam, A. G., Chan-Braun, C., Doychev, T., & Uhlmann, M. (2013). Direct numerical simulation of horizontal open channel flow with finite-size, heavy particles at low solid volume fraction. *New Journal of Physics*, *15*(2), 025031-1–025031-41.

Lajeunesse, E., Malverti, L., & Charru, F. (2010). Bedload transport in turbulent flow at the grain scale: Experiments and modeling. *Journal of Geophysical Research – Earth Surface*, *115*, F04001-1–F04001-16.

Ma, H.-B., Heyman, J., Fu, X.-D., Mettra, F., Ancey, C., & Parker, G. (2015). Bed load transport over a broad range of timescales: Determination of three regimes of fluctuations. *Journal of Geophysical Research*, *119*(12), 2653–2673. doi:10.1002/2014JF003308

Marchioli, C., & Soldati, A. (2002). Mechanisms for particle transfer and segregation in a turbulent boundary layer. *Journal of fluid Mechanics*, *468*, 283–315.

Mavis, F. T., Ho, C., Tu, Y. C., Liu, T. Y., & Soucek, E. (1935). *The transportation of detritus by flowing water (I)*. Bulletin 5, University of Iowa.

Milici, B., De Marchis, M., Sardina, G., & Napoli, E. (2014). Effects of roughness on particle dynamics in turbulent channel flows: A DNS analysis. *Journal of Fluid Mechanics*, *739*, 465–478.

Myers, W. R. C. (1978). Momentum transfer in a compound channel. *Journal of Hydraulic Research*, *16*(2), 139–150.

Nezu, I., & Nakagawa, H. (1993). *Turbulence in open-channel flows*. Rotterdam: IAHR/AIRH Monograph.

Nikora, V., Ballio, F., Coleman, S., & Pokrajac, D. (2013). Spatially averaged flows over mobile rough beds: Definitions, averaging theorems, and conservation equations. *Journal of Hydraulic Engineering*, *139*(8), 803–811.

Nikora, V., McEwan, I., McLean, S., Coleman, S., Pokrajac, D., & Walters, R. (2007). Double-averaging concept for rough-bed open-channel and overland flows: Theoretical background. *Journal of Hydraulic Engineering*, *133*(8), 873–883.

Nikora, V., McLean, S., Coleman, S., Pokrajac, D., McEwan, I., Campbell, L., & Koll, K. (2007). Double-averaging concept for rough-bed open-channel and overland flows: Applications. *Journal of Hydraulic Engineering*, *133*(8), 884–895.

Nikora, V. I., & Rowiński, P. M. (2008). Rough-bed flows in geophysical, environmental, and engineering systems: Double-averaging approach and its applications. *Acta Geophysica*, *56*(3), 529–533.

Niño, Y., & Garcia, M. H. (1996). Experiments on particle–Turbulence interactions in the near–wall region of an open channel flow: Implications for sediment transport. *Journal of Fluid Mechanics*, *326*, 285–319.

Seminara, G. (2010). Fluvial sedimentary patterns. *Annual Review of Fluid Mechanics*, *42*, 43–66.

Schlichting, H. (1960). *Boundary layer theory* (4th ed.). New York, NY: McGraw-Hill.

Shao, X., Wu, T., & Yu, Z. (2012). Fully resolved numerical simulation of particle-laden turbulent flow in a horizontal channel at a low Reynolds number. *Journal of Fluid Mechanics*, *693*, 319–344.

Shields, A. (1936). Anwendung der Ähnlichkeits-Mechanik und der Turbulenzforschung auf die Geschiebebewegung. *Preußische Versuchsanstalt für Wasserbau und Schiffbau*, *26*, 524–526. (in German).

Shiono, K., & Knight, D. W. (1991). Turbulent open-channel flows with variable depth across the channel. *Journal of Fluid Mechanics*, *222*, 617–646.

Shvidchenko, A. B., & Pender, G. (2001). Macroturbulent structure of open-channel flow over gravel beds. *Water Resources Research*, *37*(3), 709–719.

Toschi, F., & Bodenschatz, E. (2009). Lagrangian properties of particles in turbulence. *Annual Review of Fluid Mechanics*, *41*, 375–404.

Uhlmann, M. (2005). An immersed boundary method with direct forcing for the simulation of particulate flows. *Journal of Computational Physics*, *209*(2), 448–476.

Uhlmann, M. (2008). Interface-resolved direct numerical simulation of vertical particulate channel flow in the turbulent regime. *Physics of Fluids*, *20*(5), 053305-1–053305-27.

Vowinckel, B., & Fröhlich, J. (2012). Simulation of bed load transport in turbulent open channel flow. *PAMM*, *12*(1), 505–506.

Vowinckel, B., Jain, R. V., Kempe, T., & Fröhlich, J. (2016). Entrainment of single particles in a turbulent open-channel flow: A numerical study. *Journal of Hydraulic Research*, *54*(2), 158–171.

Vowinckel, B., Kempe, T., & Fröhlich, J. (2014). Fluid–particle interaction in turbulent open channel flow with fully-resolved mobile beds. *Advances in Water Resources*, *72*, 32–44.

Vowinckel, B., Kempe, T., Fröhlich, J., & Nikora, V. I. (2012). Numerical simulation of sediment transport in open channel flow. In R. M. Muñoz (Ed.), *River flow* (pp. 507–514). London: CRC Press.

Vowinckel, B., Nikora, V., Kempe, T., & Fröhlich, J. (2017). Momentum balance in flows over mobile granular beds: application of double-averaging methodology to DNS data. *Journal of Hydraulic Research*. doi:10.1080/00221686.2016.1260656

Vreman, A. W. (2007). Turbulence characteristics of particle-laden pipe flow. *Journal of Fluid Mechanics*, *584*, 235–279.

Williams, G. R. (1937). *Selected bibliography on erosion and silt movement* (Vol. *797*). Washington, DC: US Government Printing Office.

Yalin, M. S., & Ferreira da Silva, A. M. (2001). *Fluvial processes*. IAHR/AIRH Monograph, Delft, The Netherlands.